Development and Characterization of N2O-Plasma Oxide Layers for High-Temperature p-Type Passivating Contacts in Silicon Solar Cells

Libraro, Sofia; Bannenberg, Lars J.; Famprikis, Theodosios; Reyes, David; Hurni, Julien; Genc, Ezgi; Ballif, Christophe; Hessler-Wyser, Aïcha; Haug, Franz Josef; Morisset, Audrey

DOI
10.1021/acsami.4c10612

Publication date
2024

Document Version
Final published version

Published in
ACS Applied Materials and Interfaces

Citation (APA)
Libraro, S., Bannenberg, L. J., Famprikis, T., Reyes, D., Hurni, J., Genc, E., Ballif, C., Hessler-Wyser, A., Haug, F. J., & Morisset, A. (2024). Development and Characterization of N2O-Plasma Oxide Layers for High-Temperature p-Type Passivating Contacts in Silicon Solar Cells. *ACS Applied Materials and Interfaces*, *16*(36), 47931-47943. https://doi.org/10.1021/acsami.4c10612

ACS APPLIED MATERIALS & INTERFACES

www.acsami.org

Research Article

Development and Characterization of N_2O-Plasma Oxide Layers for High-Temperature p-Type Passivating Contacts in Silicon Solar Cells

Sofia Libraro,* Lars J. Bannenberg, Theodosios Famprikis, David Reyes, Julien Hurni, Ezgi Genc, Christophe Ballif, Aïcha Hessler-Wyser, Franz-Josef Haug, and Audrey Morisset*

Cite This: *ACS Appl. Mater. Interfaces* 2024, 16, 47931−47943

Read Online

ACCESS | Metrics & More | Article Recommendations | Supporting Information

ABSTRACT: Full-area passivating contacts based on SiO_x/poly-Si stacks are key for the new generation of industrial silicon solar cells substituting the passivated emitter and rear cell (PERC) technology. Demonstrating a potential efficiency increase of 1 to 2% compared to PERC, the utilization of n-type wafers with an n-type contact at the back and a p-type diffused boron emitter has become the industry standard in 2024. In this work, variations of this technology are explored, considering p-type passivating contacts on p-type Si wafers formed via a rapid thermal processing (RTP) step. These contacts could be useful in conjunction with n-type contacts for realizing solar cells with passivating contacts on both sides. Here, a particular focus is set on investigating the influence of the applied thermal treatment on the interfacial silicon oxide (SiO_x) layer. Thin SiO_x layers formed via ultraviolet (UV)−O_3 exposure are compared with layers obtained through a plasma treatment with nitrous oxide (N_2O). This process is performed in the same plasma enhanced chemical vapor deposition (PECVD) chamber used to grow the Si-based passivating layer, resulting in a streamlined process flow. For both oxide types, the influence of the RTP thermal budget on passivation quality and contact resistivity is investigated. Whereas the UV−O_3 oxide shows a pronounced degradation when using high thermal budget annealing (T > 860 °C), the N_2O−plasma oxide exhibits instead an excellent passivation quality under these conditions. Simultaneously, the contact resistivity achieved with the N_2O-plasma oxide layer is comparable to that yielded by UV−O_3-grown oxides. To unravel the mechanisms behind the improved performance obtained with the N_2O-plasma oxide at high thermal budget, characterization by high-resolution (scanning) transmission electron microscopy (HR-(S)TEM), X-ray reflectometry (XRR) and X-ray photoelectron spectroscopy (XPS) is conducted on layer stacks featuring both N_2O and UV−O_3 oxides after RTP. A breakup of the UV−O_3 oxide at high thermal budget is observed, whereas the N_2O oxide is found to maintain its structural integrity along the interface. Furthermore, chemical analysis reveals that the N_2O oxide is richer in oxygen and contains a higher amount of nitrogen compared to the UV−O_3 oxide. These distinguishing characteristics can be directly linked to the enhanced stability exhibited by the N_2O oxide under higher annealing temperatures and extended dwell times.

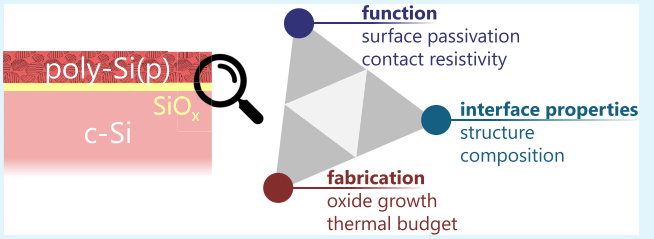

KEYWORDS: *silicon solar cells, surface passivation, poly-Si, SiO_x, PECVD, microscopy, reflectometry, photoelectron spectroscopy*

1. INTRODUCTION

The transition to full-area passivating contacts, comprising layers of silicon oxide (SiO_x) and polycrystalline silicon (poly-Si), is quickly replacing the prevailing passivated emitter and rear cell (PERC) technology in industrial silicon solar cells. Contact designs based on the TOPCon structure, employing n-type wafers with an n-type poly-Si contact on the rear and a boron-diffused p-type emitter at the front,[1] have rapidly emerged as the new industry standard. Recently, several companies reported efficiencies exceeding 26% in production with such a device structure.[2]

The fabrication process of passivating contacts typically begins with the growth of a thin SiO_x layer (approximately 1−2 nm) at the surface of the crystalline silicon (c-Si) wafer. This is followed by depositing a doped silicon layer, either polycrystalline or amorphous. Next, an annealing step is carried out to crystallize the amorphous Si (a-Si) and activate the dopants. This annealing, usually conducted between 800 and 900 °C,[1,3] or even up to 1050 °C,[4,5] with dwell times ranging between minutes to several hours, activates dopants within the poly-Si layer and facilitates their diffusion into the wafer, creating a shallow highly doped region in the c-Si. The thermal budget applied during annealing significantly affects the final passivation quality and electrical properties of poly-Si contacts.[1,6−8] In particular, several studies highlighted the importance of controlling the impact of annealing on the thin

Received: June 26, 2024
Revised: August 26, 2024
Accepted: August 26, 2024
Published: August 30, 2024

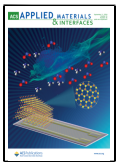

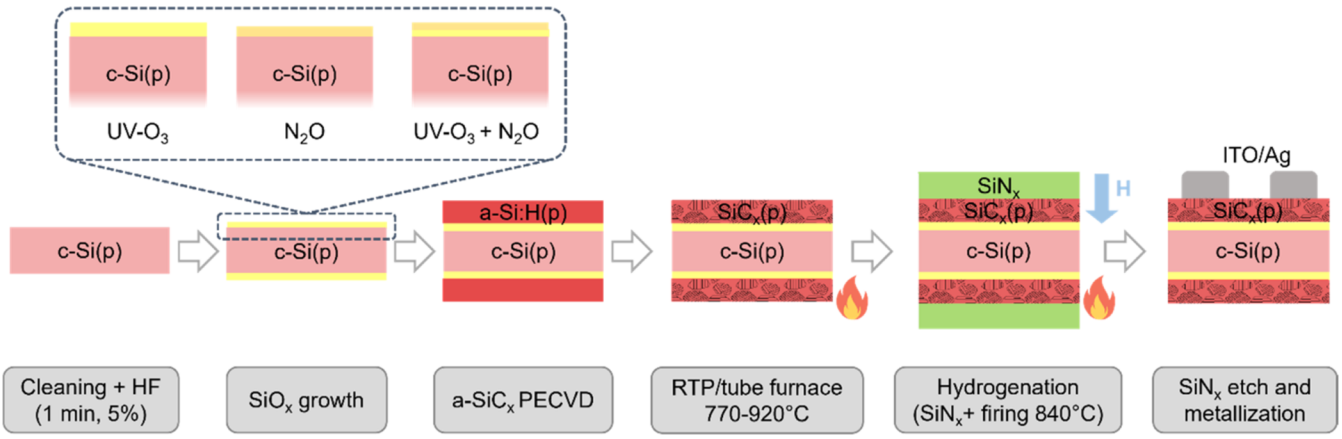

Figure 1. Schematic of the process flow employed for the fabrication of the symmetrical test samples for the presented experiments.

SiO_x layer, which undergoes chemical and structural changes during this step.[9−11]

The interfacial SiO_x can be obtained by different techniques such as chemical oxidation in hot nitric acid (HNO_3)[12,13] or in deionized water and ozone (DI-O_3);[14,15] dry oxidation with a ultraviolet (UV) excimer source or halogen lamp;[16] or thermal oxidation.[5,17−19] Except for the thermal oxidation, all of the other commonly applied techniques are based on a self-limited process where oxygen atoms penetrate the Si layers close to the surface and oxidize them.[20,21] The maximum thickness reached in this case depends on the penetration depth of oxygen atoms into the c-Si. Consequently, such oxide layers typically exhibit two distinct oxidation phases: initially, increased processing time leads to an increment in thickness until a self-saturation limit. Beyond this point, extending the processing time does not further increase thickness but instead results in the densification of the layer.[20]

Previous studies revealed that thickness and composition of the thin SiO_x layer have a strong impact on the evolution of the surface passivation with the thermal budget applied for a-Si crystallization and dopant activation: layers that are thicker or have a composition closer to SiO_2 stoichiometry proved to better withstand higher temperatures or longer dwell times. Contrarily, thinner layers with a substoichiometric composition are usually associated with a stronger degradation of the passivation at higher thermal budgets.[10,14,16] In general, dry processes such as UV-based or thermal oxidation have been found to provide higher surface passivation after annealing compared to wet chemical processes like DI-O_3 or HNO_3.[14,16,22]

Recently, several groups have investigated an oxidation process based on the exposure of the c-Si surface to an N_2O-plasma, sometimes referred to as "Plasma-Assisted N_2O Oxidation" (PANO).[23−27] This process can be performed in the same PECVD reactor used for deposition of the poly-Si and therefore allows for an easy and lean process flow to fabricate poly-Si contacts. Much like chemical oxidation or exposure to UV−O_3 radiation, N_2O-plasma oxidation is a self-limited process when only N_2O or a mix of N_2O and H_2 is added to the plasma.[28] During the initial stage of plasma exposure, the thickness increases up to a saturation level, which varies depending on certain processing parameters such as substrate temperature or plasma power, whereas for longer plasma times the thickness quickly saturates.[24] Oxides based on N_2O-plasma exhibit excellent passivation quality combined with a high stability to processing at elevated temperature.[25−27] Several reports have linked this performance with an improved oxide composition closer to the SiO_2 stoichiometry[24,26,29] and with the presence of N atoms accumulated at the Si/SiO_x interface.[27,28,30] An alternative method for growing the thin interfacial oxide via PECVD involves replacing N_2O with O_2. Recent studies have shown that this O_2-based process produces similar results to those obtained with N_2O-grown oxides when applied to n-type poly-Si contacts. However, the results also highlighted that the O_2-grown layers may be more sensitive to high annealing temperatures compared to their N_2O counterparts.[31]

Based on the promising passivation quality and thermal stability of N_2O oxides, in this contribution, we apply the N_2O-plasma oxidation process to SiO_x/poly-Si contacts formed with a rapid thermal processing (RTP) step, also referred to as fired passivating contacts (FPCs).[32] Previous studies on the impact of RTP on the passivation quality of FPCs reported very similar trends to those observed for longer annealing processes, where passivation initially improves with increasing thermal budget and then decreases beyond an optimum temperature.[33−35] As the short dwell times of RTP limit dopant diffusion across the oxide, these contacts primarily rely on dopant activation within the poly-Si layer to promote accumulation of charge carriers in the c-Si, as well as on the integrity of the SiO_x layer that provides chemical passivation.[36] In contrast to the more commonly studied n-type poly-Si layers, we focus here on p-type layers and investigate the influence of the thermal budget during RTP on contacts with oxide layers fabricated through exposure to UV−O_3, N_2O plasma, or a combination of both. To compare samples processed in different annealing set-ups, a similar investigation is conducted for p-type passivating contacts subjected to a more conventional annealing in a tube furnace instead of RTP. Additionally, the differences between UV−O_3 and N_2O-grown oxides are investigated by combining depth-dependent X-ray photoelectron spectroscopy (XPS), X-ray reflectometry (XRR), and high-resolution (scanning) TEM (HR-(S)TEM). Our analysis focuses on complete c-Si/SiO_x/poly-Si(p) stacks after RTP, which closely resemble the final structures used in solar cell applications. This approach contrasts with most existing studies that typically examine as-deposited SiO_x layers. By linking the structural and chemical properties of the oxide layers after RTP to their performance in the contacts, our work

https://doi.org/10.1021/acsami.4c10612
ACS Appl. Mater. Interfaces 2024, 16, 47931−47943

provides valuable insights for the further development and application of these contacts.

2. EXPERIMENTAL DETAILS

2.1. Sample Fabrication. The different processing steps for sample fabrication are shown in Figure 1. Symmetrical test structures were fabricated on p-type shiny-etched (SE) or double-side polished (DSP) float-zone wafers with (100) orientation. The SE and DSP wafers were 180 and 280 μm-thick, respectively, and featured a resistivity of 2 Ω·cm. After etching, cleaning, and a 1 min HF dip, samples were oxidized in three different ways. For a first group of samples, the interfacial oxide was grown by exposure to UV−O_3 for 2 min (Jelight, UVO-cleaner model 42). In the second group, the oxide was grown through a treatment in the plasma enhanced chemical vapor deposition (PECVD) chamber, using a mixture of H_2 and N_2O as precursor gases. Except if stated otherwise, a plasma treatment time and a plasma pressure of 1.5 min and 2.5 mbar were applied, respectively. For a third group, a UV−O_3 exposure of 1 min was first applied, directly followed by 1 min of N_2O-plasma treatment. After oxidation of the c-Si, a 40 nm thick a-SiC_x(p) layer was deposited by PECVD for all samples using SiH_4, H_2, CH_4 and $B(CH_3)_3$ as precursor gases (KAI-M, Unaxis). As a result of the addition of CH_4 to the precursor gas mix, the a-SiC_x layer was found in earlier work to contain about 2.5% of C.[32] The PECVD setup used for N_2O oxidation and a-SiC_x deposition consisted of a parallel plate setup with a plasma frequency of 40.6 MHz. The PECVD chamber was maintained at 200 °C during processing both the N_2O oxide and the a-SiC_x layer. Subsequently, an annealing step was applied to crystallize the layers and activate their dopants. Two different set-ups were used for performing this annealing. The first one consisted in a rapid thermal processing (RTP) system operated under N_2 ambient (Jipelec 200). With this system, set temperatures between 770 and 920 °C and dwell times between 10 and 30 s were applied, with fast heating and cooling ramps of 50 °C/s, which resulted in an overall annealing time of about 5 min. More details on this experimental procedure can be found in ref 32. The second system used for annealing consisted in a quartz tube furnace operated under Ar ambient (PEO-308, ATV Technologie). With this second setup, heating and cooling ramps of 10 and 2 °C/min were applied, respectively. The peak temperatures were 850 and 900 °C with dwell times of 0 (i.e., with the cooling ramp starting immediately after the end of the heating ramp), 15 and 30 min. After annealing, the samples were hydrogenated by depositing a layer of hydrogen-rich silicon nitride (SiN_x:H) by PECVD and then firing at a set temperature of 840 °C for a few seconds in a ceramic roller furnace (CAMINI, Meyer Burger). After hydrogenation, the SiN_x:H layers were removed by dipping the samples in a 5% HF solution. Lastly, after the HF dip, an ITO/Ag bilayer was sputtered through a shadow mask (MRC sputtering system P603, NI-HONMRC Co.) to create metallic contacts for contact resistivity measurements.

2.2. Characterization. Minority carrier lifetime and implied open-circuit voltage (iV_{oc}) were measured on unmetalized samples after hydrogenation with a Sinton WCT-100 instrument. The measurement was performed in the center of each sample. The contact resistivity of the c-Si/SiO_x/SiC_x stack was evaluated using the transfer length method (TLM). The samples were cleaved along the TLM pattern to avoid lateral current spreading. The true distances between the pads were measured by optical microscopy to account for deposition of material under the shadow masks and the current spreading into the wafer was corrected according to the two-dimensional (2D) analytical method described in ref 37 The spatial homogeneity of the passivation was investigated by photoluminescence (PL) imaging, using illumination at 808 nm and imaging with a cooled Si detector (PIXIS, Princeton Instruments).

Electrochemical capacitance−voltage (ECV) measurements were performed to evaluate the doping concentration profile in samples featuring SiO_x/SiC_x passivating layers activated through long-annealing in the tube furnace. The measurement was performed after annealing using an ECV CVP21 tool from WEP with a 0.1 mol/L NH_4F solution as etchant.

For structural and chemical characterization, DSP wafers were used to allow for minimal roughness at the c-Si/SiO_x/SiC_x interface. X-ray photoelectron spectroscopy (XPS) measurements were performed with a ThermoFisher K-α spectrometer. The base pressure in the analysis chamber was approximately 2×10^{-9} mbar. Etching was performed using an Ar^+ ion gun operated at 2 keV. The spot size was approximately 800×400 μm^2. On each sample, three points were measured. Full depth profiling was performed by stepwise etching in 5 and 10 s steps. The etching rate was approximately of 0.2 nm s^{-1} as determined by XRR measurements (see next paragraph). At each step, measurements were performed with the pass energy set to 150 eV ("Snap" mode). For the third spot, one measurement was performed after 180 s of etching, and subsequently a scan was made from 210 to 240 s of etching. At these points detailed high-resolution scans with the pass energy of the analyzer set to 50 eV ("Scan" mode) were performed. In the analysis, the binding energy was corrected for the 0.3 eV charge shift using the primary C 1s hydrocarbon peak at BE = 284.8 eV as a reference. The data were fitted using 70% Gaussian and 30% Lorentzian line shapes (weighted least-squares fitting method) and nonlinear Shirley-type background using the ThermoFisher Avantage software.

X-ray reflectometry (XRR) measurements were performed to study the structural composition of the samples and get estimates on the thickness, density and roughness of each of the layers. This technique can be used for flat samples with layer thickness between approximately 1−500 nm. In XRR, the sample is illuminated with X-rays and the reflectivity of these X-rays is measured as a function of 2θ. Typically, instead of displaying the reflectivity as a function of 2θ, the reflectivity is displayed as a function of the momentum transfer $Q = 4\pi \sin\theta/\lambda$ to take into account the effect on the X-ray's wavelength. The proportion of X-rays reflected, i.e., the reflectivity, depends on the scattering length density (SLD)

$$\mathrm{SLD} = \sum_{i=1}^{n} N_i f_i(0)$$

where N_i and f_i are the atomic number density (number of atoms per volume unit) and the atomic form factor of isotope i. In good approximation, $f_i(0)$ is proportional to the number of electrons, and as such the SLD for X-rays is proportional to the electron density of the material. Analogues to the reflection of optical light by a material (Fresnel reflection), the X-rays can be reflected by the surface of the thin film, or by the interface between the layers present in the thin film. This can result into an interference pattern with minima and maxima, named fringes, where the periodicity of these fringes is inversely related to the thickness of the layers, and the amplitude to the difference in SLD between the layers (i.e., the difference in electron density). In addition, a higher roughness can also dampen the fringes. To disentangle between these effects and get reliable estimates for the thickness, SLD and roughness of each layer, XRR data is typically fitted using a model that describes each layer within the film. Based on this, an SLD profile can be constructed, which displays the SLD as a function of the vertical distance from the substrate. This SLD profile can be interpreted as an electron density profile of the thin film stack. The XRR experiments were performed with a Bruker D8 Discover (Cu Kα, λ = 0.154 nm) on samples that were approximately 10×15 mm^2 in size. Measurements were performed for the range $0° < 2\theta < 2°$ with a 0.1 mm Cu absorber and for $0.5° < 2\theta < 5°$ without an attenuator. This was done to avoid saturation and to ensure linearity of the detector in the angular range where the reflected intensity is high. The two measurements for each sample were subsequently stitched using a custom Python code. The data was analyzed with GenX 3.6.20 software,[38] using a model with two layers (corresponding to SiO_x and SiC_x) on top of a c-Si substrate. In the analysis, the properties of the bulk Si (thickness, density and roughness) were kept constant, as well as the thickness of the SiO_x layer. This was done to improve the fit quality, as in a previous analysis performed on very similar sample structures, a strong

https://doi.org/10.1021/acsami.4c10612
ACS Appl. Mater. Interfaces 2024, 16, 47931−47943

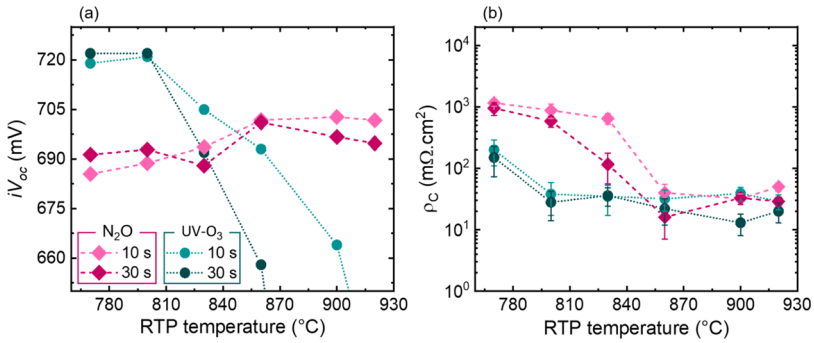

Figure 2. Dependence of the iV_{oc} after hydrogenation (a) and of the contact resistivity (ρ_C) (b) on the RTP temperature for dwell times of 10 and 30 s, for samples with UV−O_3 (green circles) and N_2O (pink diamonds) oxide layers. The error bars in (b) denote the standard deviation over 4 different samples.

correlation was found for thickness and density of the SiO_x layer.[39] Therefore, the free parameters in the fit were the density, roughness and thickness associated to the SiC_x and the density and roughness associated to the SiO_x layer.

Transmission electron microscopy (TEM) was performed on a selection of samples. For this purpose, focused ion beam (FIB) was used to prepare thin lamellae with the standard lift-out method (Zeiss NVision). The samples were then observed both in high-resolution TEM and high-resolution scanning TEM (HR-STEM) mode in a double spherical aberration (Cs) corrected Titan Themis microscope (ThermoFisher Scientific) with an accelerating voltage of 200 kV.

3. RESULTS AND DISCUSSION

3.1. Impact of Thermal Budget on Functional Properties of Poly-Si Contact. In this section, we present the effect of the annealing thermal budget applied for crystallization and dopant activation of the a-SiC_x(p) layer on the surface passivation properties of the resulting passivating contact. The thin SiO_x layer located at the interface between the SiC_x and the c-Si substrate was grown either by UV−O_3, N_2O-plasma or a combination of both. In the first two Sections 3.1.1 and 3.1.2, the annealing was performed in a RTP furnace with an overall processing time of about 5 min. In the third Section 3.1.3, the annealing was performed in a tube furnace with an overall processing time of about 3 h. For both annealing set-ups, the thermal budget was varied by changing the dwell temperature and dwell time.

3.1.1. Effects of RTP Thermal Budget. In this section, we present results on the influence of the RTP thermal budget on the passivation and electrical transport properties of contact stacks featuring UV−O_3 and N_2O-grown oxide layers. Figure 2a depicts implied V_{oc}(iV_{oc}) values measured after hydrogenation for samples featuring the two different oxide types, for different RTP temperatures and dwell times. We note that each iV_{oc} data point refers to a single measurement performed on a sample under each condition. The samples featuring UV−O_3-grown SiO_x show a passivation quality initially stable until T = 800 °C, followed by a decline toward higher temperatures. This drop could be explained by the creation of interfacial defects across the oxide, which become detrimental for higher temperatures or longer dwell times,[35] or even by the disruption of the oxide layer for the highest thermal budgets. For the longest dwell times (30 s) the observed drop in the passivation is stronger, suggesting that the onset of oxide disruption is shifted to lower temperatures if the dwell time is increased.

In prior work, we emphasized the importance of employing a higher thermal budget for contacts formed by RTP to ensure sufficient lateral conductivity of the poly-Si layers and compatibility with localized metal contacts.[40] However, the results of Figure 2a demonstrate that UV−O_3-grown oxides do not provide high enough surface passivation in the range of high thermal budget. Therefore, an oxide layer based on exposure to N_2O-plasma in the PECVD chamber was developed with the goal of obtaining improved stability for the surface passivation at high temperatures and longer dwell times, and thus accessing the high thermal budget range. We note that, in the early developments of the N_2O oxide layer, the addition of H_2 to the precursor gas mix was observed to improve the spatial homogeneity of the oxidation (assessed by PLI); H_2 was thus systematically added in following optimization stages. Additional results on the optimization of plasma time and pressure during PECVD for the N_2O oxidation process are available in Supporting Information, Figures S1 and S2.

Looking at the iV_{oc} values after hydrogenation displayed in Figure 2a, it is clear that the N_2O-plasma oxide exhibits a completely different trend with temperature when compared to the previously studied UV−O_3 oxide layer. In particular, no steep decrease of iV_{oc} toward high temperatures or longer dwell times is noticed. Rather, the passivation improves as the thermal budget increases and remains stable above 700 mV for dwell times of 10 s. For longer dwell time, only a slight decrease in iV_{oc} occurs above 860 °C. These results highlight the superior passivating performance at high thermal budget of the N_2O-plasma oxide compared to the UV−O_3 one. We note that the spatial homogeneity of the passivation quality, assessed by photoluminescence imaging (PLI), was observed to be comparable for both N_2O and UV−O_3 oxides under optimal conditions, as shown in Supporting Information, Figure S4.

Figure 2b illustrates the dependence of the contact resistivity on the RTP temperature and dwell time. The two sample series with UV−O_3 oxides exhibit higher contact resistivity for RTP temperatures below 800 °C, followed by a drop to values below 60 mΩ·cm². The substantial decrease in contact resistivity can be attributed to a higher density of active dopants in the SiC_x layer when processed at higher temperatures, which, in turn, influences the resistivity at both the c-Si/SiO_x/SiC_x and SiC_x/metal interfaces.[33,35,40] The N_2O-plasma oxide also shows a similar behavior, but the drop in ρ_C occurs at higher temperatures compared to the UV−O_3 oxides, specifically at T > 830 °C for 30 s dwell times and T > 860 °C for 10 s. Interestingly, despite the initial contact resistivity being one order of magnitude higher than that of UV−O_3 oxide, it eventually achieves values within the same range as UV−O_3 oxides at high thermal budgets. In combination with

https://doi.org/10.1021/acsami.4c10612
ACS Appl. Mater. Interfaces 2024, 16, 47931−47943

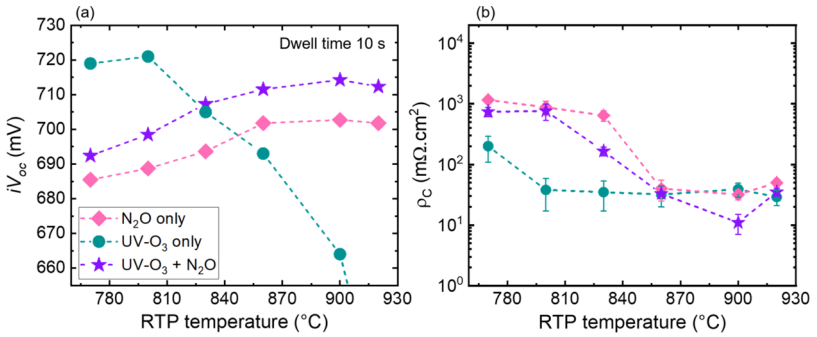

Figure 3. Implied V_{oc} (iV_{oc}) values after hydrogenation (a) and contact resistivity results (b) for N_2O only (pink diamonds), $UV{-}O_3$ only (green circles) and $UV{-}O_3$ + N_2O (purple stars) as a function of RTP temperature, for dwell times of 10 s. The error bars in (b) denote the standard deviation over 4 different samples.

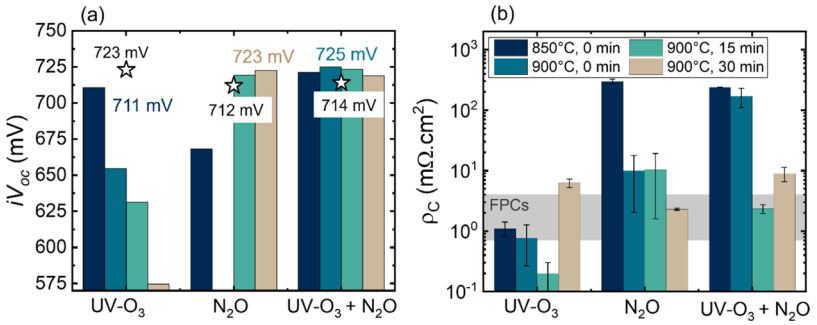

Figure 4. Implied V_{oc} (iV_{oc}) after hydrogenation (a) and contact resistivity (b) results for layers featuring a $UV{-}O_3$, N_2O and a combination of both oxides and annealed in a tube furnace with different annealing temperature and dwell times. The iV_{oc} data point relative to the N_2O oxide with 900 °C, 0 min annealing is missing due to a damaged sample. To facilitate comparison with the RTP annealed samples, in (a), the best results obtained with RTP on each oxide type are indicated by the white stars (for optimized conditions). In (b), the typical range of contact resistivities achieved with optimized RTP conditions is highlighted by the gray-shaded area. The error bars denote the standard deviation over 2 or 3 different samples.

the high passivation quality, this makes the N_2O-plasma oxide an excellent option for implementing in passivating contacts processed by RTP at high thermal budgets.

3.1.2. Combination of $UV{-}O_3$ and N_2O Oxides. In the previous section, Figure 2a showed that the optimum $UV{-}O_3$ oxide yields higher iV_{oc} values compared to the best results obtained with the N_2O-plasma oxide at low thermal budget (iV_{oc} = 722 mV for $UV{-}O_3$ compared to 705 mV for the N_2O oxide). Therefore, a combination of $UV{-}O_3$ and N_2O oxides was investigated to combine the excellent passivation quality exhibited by the $UV{-}O_3$ oxide at low thermal budgets with the superior tolerance for high thermal budgets demonstrated by the N_2O-plasma oxide.

Figure 3a illustrates the iV_{oc} as a function of RTP temperatures for dwell times of 10 s (additional results on samples processed with RTP dwell times of 30 s are available in Supporting Information, Figure S3). The graph compares a set of samples featuring only the N_2O-plasma oxide and only the $UV{-}O_3$ oxide (reproduced from Figure 2a) with the third set that received both $UV{-}O_3$ exposure and N_2O-plasma treatment.

Both samples with N_2O-only and $UV{-}O_3$ + N_2O oxide layers exhibit a similar trend with respect to the passivation quality, with iV_{oc} improving as the RTP temperature increases. However, the combination of $UV{-}O_3$ and N_2O oxides consistently demonstrates higher iV_{oc} values, approximately 10−15 mV higher than the N_2O-only samples across the entire temperature range investigated here. Similarly to the N_2O-only samples, the spatial homogeneity of the passivation provided by the $UV{-}O_3$ + N_2O oxide layers under optimized RTP conditions is comparable to that of the optimized $UV{-}O_3$ oxide layer (see Figure S4 in the Supporting Information).

Contact resistivity results for the three sample types are presented in Figure 3b. Interestingly, the drop of contact resistivity is shifted to slightly lower temperatures for the $UV{-}O_3$ + N_2O layer, compared to the N_2O-only (T > 830 °C compared to 860 °C). For T > 860 °C, however, both N_2O-based oxides yield similar results, which are also comparable to the contact resistivity values obtained with the $UV{-}O_3$ only oxide layers.

3.1.3. Application of the Plasma Oxide to Long-Annealed $SiC_x(p)$ Layers. Most commonly, the annealing for a-Si crystallization and dopant activation is performed in a tube furnace. Compared to the RTP system used here, annealing in tube furnace involves longer ramp-up and ramp-down times, resulting in overall processing of several hours (in contrast to a few minutes with RTP). To compare the properties of passivating contacts annealed in different set-ups, we fabricated similar $SiO_x/SiC_x(p)$ passivating contacts featuring the three investigated oxide types and annealed in a tube furnace instead of RTP. We note that in this experiment, the N_2O oxide was grown using a plasma pressure of 2 mbar and a plasma treatment time of 1 min. In the tube furnace, the peak temperatures were 850 and 900 °C with dwell times of 0 (i.e., with the cooling ramp starting immediately after the end of the heating ramp), 15 and 30 min. The results are summarized in Figure 4. Overall, the trends exhibited by the different types of samples closely resemble the results obtained with the RTP.

https://doi.org/10.1021/acsami.4c10612
ACS Appl. Mater. Interfaces 2024, 16, 47931−47943

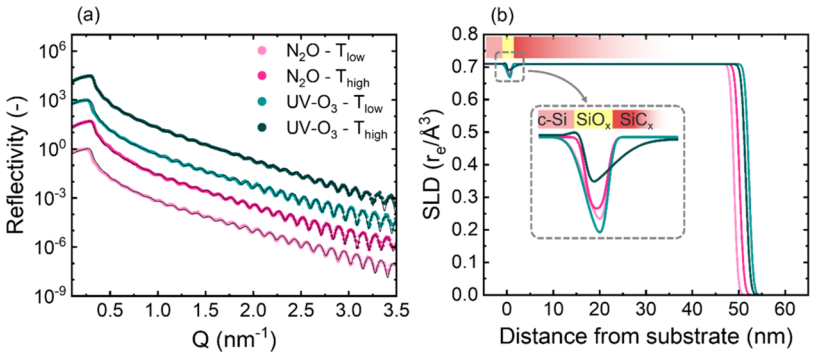

Figure 5. X-ray reflectograms (experimental data points and fit, vertically offset for clarity) of the four studied samples (a) and associated SLD plot obtained from fitting the reflectograms data (b). The abscissa represents the distance from the surface of the c-Si wafer; the position of the different layers in the stack is indicated by the color bars at the top of the graph. The inset shows a focus on the position of the SiO_x interfacial layers.

In particular, the UV−O_3 oxide exhibits the best iV_{oc} of 711 mV at the lowest thermal budget, with a steep decrease of the passivation quality for increasing temperature and dwell time, likely due to the disruption of the oxide layer. In contrast, both the N_2O and the UV−O_3 + N_2O combination outperform the UV−O_3 oxide over most of the studied range, yielding high iV_{oc} values of 723 and 725 mV, respectively. The N_2O-only oxide shows an improving passivation quality with increasing thermal budget, as in the case of passivating contacts processed by RTP. As previously discussed, this can be explained with the improved field-effect passivation, in this case also due to the shallow in-diffusion of B dopants within the c-Si substrate. Similarly to the case of samples processed by RTP, the combination of the UV−O_3 and N_2O oxides yields the best results in terms of iV_{oc} and exhibits a constant passivation quality over the full range of applied thermal budgets. The active doping profile of these samples was evaluated by ECV after annealing. For all annealing conditions, we observed a deeper B in-diffusion in the c-Si for samples featuring a UV−O_3-grown oxide compared to samples exposed to N_2O-plasma or a combination of UV−O_3 and N_2O (see Figure S5 in Supporting Information). These observations agree well with previous reports showing that oxide layers obtained through N_2O-plasma treatments can hinder B diffusion into the wafer, resulting in shallower in-diffused region at the c-Si surface of these samples compared to the ones featuring UV−O_3 oxides.[26,27,29] This could explain why a higher thermal budget is needed to fully activate the contacts featuring the N_2O oxide compared to the UV−O_3 one. The combination of both oxides likely corresponds to an in-between situation, thus showing excellent performance at both low and high thermal budgets.

The contact resistivity values for the three types of interfacial oxides are displayed in Figure 4b. Once again, the observed trends are close to those presented for the samples annealed in RTP. The UV−O_3 oxide shows an overall trend of decreasing contact resistivity with increasing thermal budget. The higher ρ_C for the 900 °C, 30 min annealing of the UV−O_3 sample could be related to a thicker parasitic oxide at the surface of the SiC_x layer, not fully removed by the HF dip performed before metalization.[40] Both the N_2O and UV−O_3 + N_2O oxides show high contact resistivity at lower temperatures/shorter dwell times, and a drop for higher thermal budgets.

Overall, both RTP and tube furnace processes yield comparable results for passivation and contact resistivity in SiC_x(p) layers, highlighting the versatility of plasma oxidation. Utilizing N_2O-plasma oxidation, potentially combined with UV−O_3 treatment, offers a promising route to enhance electrical properties at high thermal budgets while maintaining high surface passivation quality. Additionally, it offers the possibility of fabricating SiO_x/poly-Si contacts using PECVD for both layer depositions.

3.2. XPS, XRR, and TEM Investigation of N_2O and UV−O_3 Oxides. In this section, the reasons underlying the superior passivation performance of the N_2O-plasma oxide at high thermal budgets are investigated by means of high-resolution transmission electron microscopy (TEM), X-ray reflectometry (XRR) and X-ray photoelectron spectroscopy (XPS). For this study, passivating contacts featuring UV−O_3 and N_2O oxide are characterized, and the following RTP conditions are compared for both type of oxides:

- T_{low} = 830 °C, dwell time of 3 s, corresponding to the optimum condition for the UV−O_3 oxide, optimized in previous work.[33,35]
- T_{high} = 860 °C, dwell time of 30 s, corresponding to the window of parameters where the N_2O oxide shows high passivation quality whereas the UV−O_3 oxide yields low iV_{oc} (see Figure 2).

3.2.1. Structural Characterization. Figure 5a shows the reflectograms of the four investigated samples featuring different oxide layers and RTP thermal budgets. The periodic fringes result from the regular pattern of destructive and constructive interference of the X-rays reflected at the different interfaces. In particular, the period of the oscillations is related to the thickness differences between the layers in the sample, whereas the amplitude is related to their density difference (i.e., the higher the fringes' amplitude, the higher the density difference between the layers).

In a recent study, XRR was employed to characterize samples closely resembling those investigated in this work.[39] It was found that within the temperature range relevant to our study, the density of the SiC_x layer closely approximates that of crystalline silicon (c-Si). Consequently, the fringes observed in the reflectogram primarily arise from the contrast induced by the presence of the thin SiO_x layer at the interface between c-Si and SiC_x. In the plot of Figure 5a, the amplitude of the fringes for the N_2O samples and the UV−O_3 sample processed at T_{low} is larger than for the case of the UV−O_3 sample processed at T_{high}. This observation suggests a stronger density contrast between the c-Si, SiO_x, and SiC_x layers for the former case. Conversely, the high thermal budget UV−O_3 sample displays fringes featuring reduced amplitude, which could indicate a less

https://doi.org/10.1021/acsami.4c10612
ACS Appl. Mater. Interfaces 2024, 16, 47931−47943

defined interface with higher roughness, or a smaller density contrast compared to the other samples.

In Figure 5b, the fit of the reflectograms is plotted as a scattering length density (SLD) profile as a function of the distance from the c-Si substrate. As the SLD of X-rays is roughly proportional to the mass density, this type of plot represents the density of the different layers (here SiO_x and SiC_x) and changes between the different phases in a multilayer stack. The different fitted values (namely, thickness, SLD and roughness) respective to the SiO_x and SiC_x layers are also featured in the Supporting Information, Table S1.

In Figure 5b, a slight difference in the thickness of the SiC_x layer among the four samples can be observed, ranging from 48 to 51 nm, which could be attributed to the fact that these layers were not deposited in the same PECVD run but in consecutive ones. The inset of Figure 5b zooms in on the SLD plots in the area of the interfacial oxides. The four samples display an effective difference in the density of the SiO_x layers. In particular, the samples processed at T_{high} show a density that is closer to the one of the c-Si silicon. This observation is consistent with other reports of densification of silicon oxide layers upon high temperature treatment.[10,39] Most importantly, the plot suggests that the N_2O oxide only undergoes limited changes in density when processed at high thermal budget, whereas the two UV−O_3 samples processed at T_{low} and T_{high} show a marked difference. In particular, an increase in density can be observed for the UV−O_3 sample processed at T_{high}. Furthermore, the interval in which the density drops at the SiO_x/SiC_x interface is larger for this sample, which indicates a larger roughness at this interface in comparison to the other samples. This could be interpreted as the sign of more intermixing at the interface between the SiO_x and SiC_x layers for this sample.

These observations, directly linked to the reduced amplitude of the fringes observed in the reflectogram of the UV−O_3 sample processed at T_{high} in Figure 5a, suggest that the SiO_x/SiC_x interface for this oxide layer is rougher than in the other samples, with SiO_x being intermixed with the c-Si and SiC_x(p) layers. This is likely a consequence of RTP, which supposedly leads to the partial disruption of the UV−O_3 oxide. This result could thus explain the loss of passivation at high thermal budgets observed previously. In contrast, the SLD plot for the N_2O sample processed at T_{high} reveals a well-defined layer, and only small changes can be observed between the low and high thermal budget samples. This suggests that the plasma oxide maintains its structural integrity even when undergoing postprocessing at high temperatures.

The two different samples featuring UV−O_3 and N_2O-grown oxides and processed at high thermal budget (T_{high}) were also characterized by high-resolution TEM and STEM-high-angle annular dark-field imaging (STEM-HAADF) in order to gain further insights into the differences observed in XRR. Figure 6 displays low magnification (a, b) and high magnification (c, d) HR-TEM micrographs of the samples with N_2O and UV−O_3 oxides.

For the N_2O-plasma oxide (a, c) the c-Si/SiO_x/SiC_x interface appears uniform, featuring a continuous SiO_x layer that is clearly distinguishable from the silicon wafer and the SiC_x. The thickness of this layer can be estimated to be approximately 1.4−1.5 nm from the micrograph, and its amorphous nature is evident. In contrast, the UV−O_3 sample shows a markedly rough and discontinuous interface, with the SiO_x layer being not clearly visible. Moreover, certain areas,

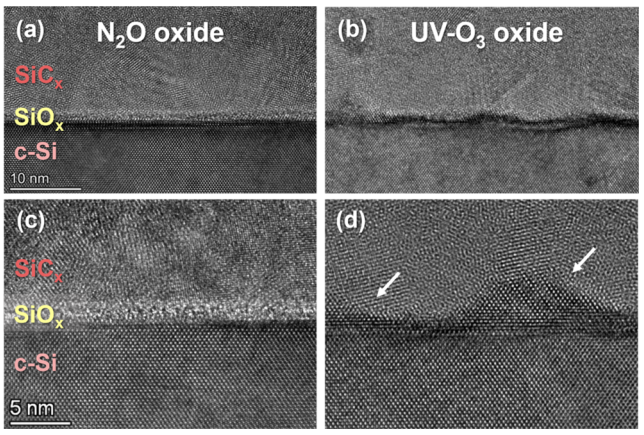

Figure 6. High-resolution TEM micrograph showing the c-Si/SiO_x/SiC_x(p) interface in the case of the N_2O-plasma oxide (a) and UV−O_3 oxide (b), for the same RTP temperature of 860 °C and a dwell time of 30 s. Higher magnification of the interface is shown in (c, d). White arrows in (d) highlight the presence of crystalline protrusions at the position of the interfacial SiO_x for the case of the UV−O_3 oxide.

indicated by the white arrows in Figure 6d, exhibit lattice fringes at the position of the SiO_x layer. These correspond to regions where the oxide layer is locally disrupted, bringing the c-Si in direct contact with the SiC_x(p) layer, and with Si crystallites epitaxially formed into the SiC_x layer.

Similar features are evident in the STEM-HAADF micrographs of Figure 7. In Figure 7a, the SiO_x layer is clearly visible

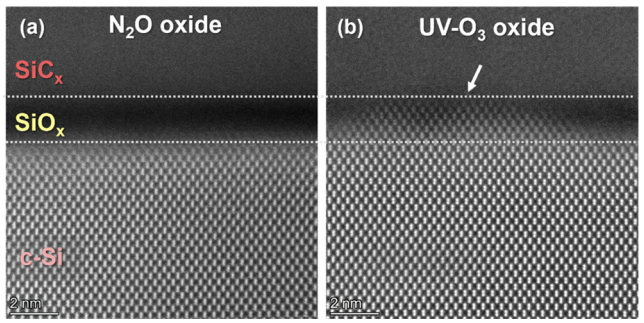

Figure 7. High-resolution STEM-HAADF micrographs showing the c-Si/SiO_x/SiC_x(p) interface in the case of the N_2O-plasma oxide (a) and UV−O_3 oxide (b), for the same RTP temperature of 860 °C and a dwell time of 30 s. The white arrow in (b) highlights the presence of crystalline protrusions at the position of the interfacial SiO_x for the case of the UV−O_3 oxide. The SiO_x position is highlighted by the white dotted lines.

due to the darker contrast (arising from a difference in atomic number) and extends continuously over the entire interface. In Figure 7b, a high-magnification micrograph of one of the regions where the UV−O_3 oxide is interrupted highlights atomic columns aligned epitaxially with the c-Si layer at the SiO_x position. The darker contrast typical of the SiO_x layer is still visible at the region of the crystalline protrusion, likely due to a superposition of regions where the oxide remains intact and the region with the pinhole. These observations are also supported by STEM-electron energy loss spectroscopy (STEM-EELS) elemental maps presented in Supporting Information, Figure S6.

The observations reported here align well with the results obtained from XRR, which revealed a less defined SiO_x layer,

https://doi.org/10.1021/acsami.4c10612
ACS Appl. Mater. Interfaces 2024, 16, 47931−47943

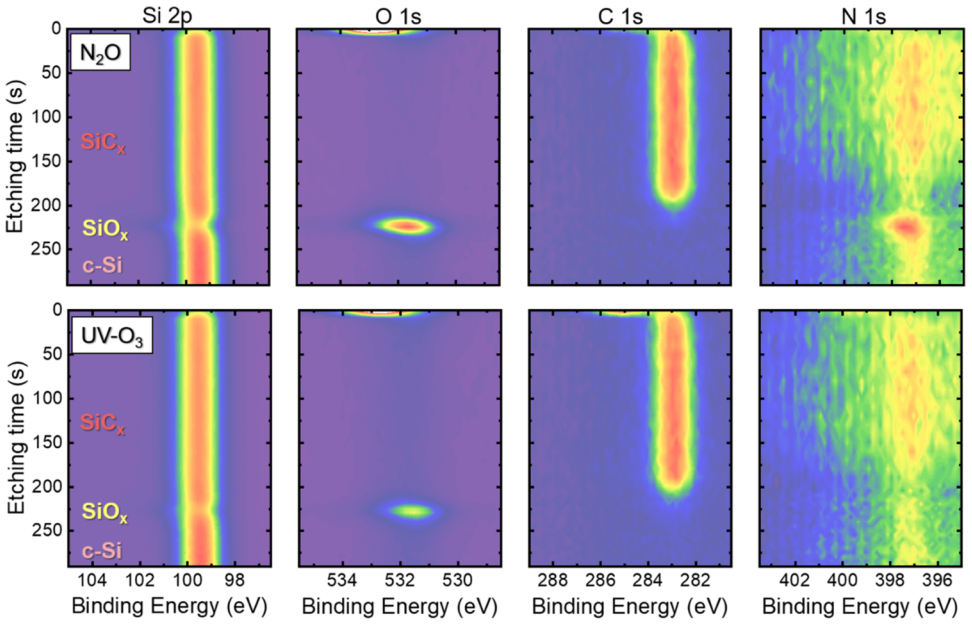

Figure 8. Contour plots showing the signal intensity as a function of etching time and binding energy for the Si 2p, O 1s, C 1s, and N 1s spectral ranges. The first row shows the data relative to the N_2O oxide and the second one to the UV−O_3 at T_{low} for both samples. The position of the c-Si, SiO_x, and SiC_x layers is indicated on the left side of the Si 2p graph. The intensity scale is the same for the plots relative to the same spectral range for the two samples, but changes for each of the displayed spectral ranges.

intermixed with the c-Si and SiC_x for the case of the UV−O_3 sample annealed at T_{high}. Conversely, a clear contrast was observed between the N_2O-grown oxide and both the silicon wafer and the SiC_x layer. Following the observations by electron microscopy discussed above, the vanishing of XRR fringes for the UV−O_3 can be linked to the local disruption of the SiO_x layer and the direct contact between the c-Si and the SiC_x.

On the contrary, the N_2O-grown oxide is observed to maintain its structural integrity after RTP, both at the microscopic scale (nm; probed with TEM) and the average scale (mm^2; probed with XRR).

We note here that several HR-TEM and STEM-HAADF micrographs were acquired at different locations during the experiment. The UV−O_3 oxide disruption and the integrity of the N_2O oxide layer were consistently observed across the entire area of the lamella. However, given the limited dimensions of the lamella (approximately 10−15 μm), caution should be exercised when generalizing these microscopic observations to the entire interface. The combination of TEM with additional XRR analysis mitigates this limitation of the TEM technique, since XRR enables probing a much larger sample surface. The consistent results obtained from both techniques thus allow us to more confidently extend our conclusions to the entire samples' surface.

3.2.2. Depth-Dependent XPS Analysis. To investigate whether the observed differences in XRR and TEM results were linked to the composition of the oxide layer and the local bonding environment of the silicon atoms within, XPS measurements were conducted on the four previously described samples. Depth-profiles were recorded throughout the full c-Si/SiO_x/SiC_x stacks, by alternating etching steps with Ar ions and XPS measurements.

Figure 8 displays contour plots for the UV−O_3 and N_2O samples that underwent RTP at the low thermal budget of T_{low} = 830 °C, for 3 s dwell time. The color map represents signal intensity as a function of the etching time and binding energy for four different spectral ranges: Si 2p, O 1s, C 1s, and N 1s.

At etching time t_{etch} = 0 s a peak in the intensity of the O 1s signal is visible for both samples, indicating the presence of a native oxide on top of the SiC_x surface. For longer etching times, both a peak in the Si 2p and C 1s signals are detected, indicating the presence of the SiC_x layer. The C 1s peak shows a sudden decrease in intensity for $t_{etch} \approx 220$ s, coinciding with a peak in the intensity of the O 1s signal. This marks the position of the SiO_x layer, which is also visible from a slight shift of the Si 2p signal toward higher binding energy for $t_{etch} \approx$ 225 s, hinting at the presence of a SiO_x phase. For $t_{etch} > 225$ s, only the Si 2p peak signal is detected, indicating that the c-Si wafer has been reached. These observations are valid both for the N_2O and UV−O_3 oxide.

The main difference between the two samples can be observed by comparing the plots related to the N 1s signal, where the N_2O oxide exhibits a peak for $t_{etch} \approx 225$ s that is absent in the UV−O_3 sample. We note that the relatively intense N 1s background, observed in particular in the SiC_x layer, could result from the Ar gas used for sputtering, which could be contaminated with N. Alternatively, it could be attributed to a contamination of the Ar gas used to create an inert atmosphere during RTP. To distinguish between these effects, it may be beneficial to record XPS depth profiles on as-deposited c-Si/SiO_x/SiC_x samples. Nonetheless, the increase in N 1s signal intensity in the vicinity of the SiC_x/c-Si interface for the plasma oxide sample compared to the absence of such a peak in the UV−O_3 oxide sample is evident.

This finding demonstrates the presence of N in the oxide obtained by N_2O-plasma after annealing in RTP. To the best of our knowledge, this is the first time the presence of N is evidenced in the thin N_2O oxide embedded in the SiO_x/poly-Si passivating stack subjected to annealing at high temperature. In previous reports, the presence of N in oxides obtained with a very similar process was observed on as-deposited SiO_x

https://doi.org/10.1021/acsami.4c10612
ACS Appl. Mater. Interfaces 2024, 16, 47931−47943

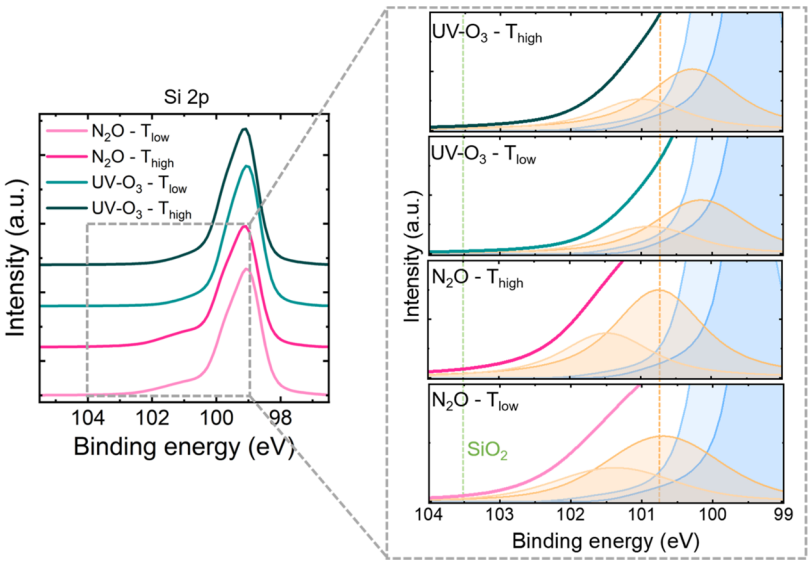

Figure 9. Fitted XPS signal in the Si 2p spectral range for the four samples included in the study. The right panel zooms-in on the area of the shoulder in the XPS signal highlighted by the gray rectangle. In the right panel, the thick colorful lines correspond to the fitted XPS signal. The pair of peaks used to fit the elemental Si peak is displayed in blue, the pair of peaks used to fit the SiO_x peak in orange. The orange dashed line highlights the shifted positions of the SiO_x peaks for the N_2O samples compared to the UV−O_3 samples. The green dashed line indicates the position of the characteristic SiO_2 peak at BE = 103.5 eV.[41]

layers, where it was linked to a reduced interfacial defect density and a reduced dopant diffusion in the c-Si after annealing compared to oxide layers obtained with other methods.[25,27,28,30]

The discussion of the XPS depth profile in this section was conducted for samples processed at T_{low}. However, similar features were observed in the depth profiles of the two samples processed at T_{high}, which are shown in the Supporting Information, Figure S7.

To further investigate the differences in the four samples, the data relative to the Si 2p range at the position of the thin oxide layers are presented in Figure 9. Here, an intense peak at BE ≈ 99 eV, corresponding to elemental Si, can be observed for all samples. The small amount of C present in the SiC_x(p) layer (≈2.5 atom %[32]) is not observed to affect the peak position in this case. No peak is observed for BE = 103.5 eV, characteristic to SiO_2.[41] However, a shoulder of variable intensity is observed for all four samples, which indicates the presence of a substoichiometric oxide layer SiO_x. Notably, the two samples featuring a N_2O oxide exhibit a more pronounced shoulder in the region around ≈101−102 eV, which is less prominent in the UV−O_3 samples. The right panel zooms-in in the area of BE = 99−104 eV and depicts the XPS fitted signal along with the doublets of peaks employed for the fitting in the Si 2p range. Specifically, the doublet representing the SiO_x states is highlighted in orange in the plots. The positions of these two peaks provide insights into the oxidation state of silicon, and consequently, the composition of the oxide layers.[42−44] We note that the fits of the XPS signals are not reproduced in the full Si 2p range in left panel of Figure 9 for clarity; however, they are featured in the Supporting Information (Figure S8) along with the fits in the O 1s and N 1s ranges.

It is evident from Figure 9 that the samples with the N_2O-plasma oxide exhibit a shift toward higher energies in the SiO_x doublet. This shift suggests a difference in the composition of the N_2O oxide layer, which appears to be closer to a SiO_2 stoichiometry (peak at 103.5 eV),[41] and hence richer in oxygen, compared to its UV−O_3 counterpart. Overall, the XPS results indicate a significant difference in the composition of the thin oxides grown by exposure to N_2O plasma or UV−O_3, with the N_2O oxide containing nitrogen and a higher amount of oxygen compared to its UV−O_3 counterpart.

3.3. Discussion. In this final section, we compare and discuss the results obtained from characterizations presented in Section 3.2 with the functional properties described in Section 3.1. Overall, the results obtained from the combined characterization techniques are consistent with the passivation quality and contact resistivity data presented in the previous sections. As shown in Sections 3.1.1 and 3.1.2, the passivation quality of samples with UV−O_3 interfacial oxide deteriorates significantly after RTP at high thermal budgets. The results obtained from XRR and TEM characterization shown in part 3.2.1 allow us to correlate this decrease in passivation quality with the structural degradation of the UV−O_3 oxide along the interface. In contrast, the passivation quality of samples with N_2O-interfacial oxide remained stable at high thermal budget, indicating that this layer features a higher tolerance to elevated temperature and prolonged dwell time. The results of the XRR and TEM characterizations allow us to confirm that the N_2O-oxide layer maintain its structural integrity along the interface under an extended range of thermal budgets compared to the UV−O_3 oxide.

The results from XPS characterization shown in part 3.2.2 enable hinting that this distinct behavior between the two oxides arises from differences in their composition and local bonding environments. Specifically, the higher oxygen content and the presence of nitrogen in the N_2O-oxide likely contribute to its increased thermal stability, possibly because of stronger bonds present at the interface with the c-Si wafer. A link between high-temperature stability and the stoichiometry of the oxide layer has been highlighted in previous research: oxide layers that are oxygen-rich (i.e., close to SiO_2 stoichiometry) have generally demonstrated better resistance to high-temperature processes compared to substoichiometric,

https://doi.org/10.1021/acsami.4c10612
ACS Appl. Mater. Interfaces 2024, 16, 47931−47943

silicon-rich oxide phases.[10,16] Our findings regarding N_2O-plasma and UV−O_3 oxides are aligned with these observations, and the improved surface passivation provided by the N_2O-oxide at high temperatures could indeed be linked to its oxygen-rich composition. Furthermore, recent studies suggest that the presence of nitrogen in N_2O plasma oxides could explain their superior performance in passivating the c-Si surface, either by blocking excessive dopant diffusion across the oxide or by improving the ability of nitrogen-containing oxide layers to retain hydrogen during high-temperature processes.[25,27]

The similar trends observed for the N_2O-only and UV−O_3 + N_2O oxides suggest that the latter also possesses a higher nitrogen and oxygen content compared to the pure UV−O_3 oxide. The addition of the N_2O treatment on top of the UV−O_3 oxide may lead to incorporation of O and N in the latter, which explains the improved thermal stability yielded by the UV−O_3 + N_2O combination. However, to confirm this hypothesis, it would be necessary to repeat the same analysis presented in Section 3.2 on the combined oxide layers as well.

The reason why the optimized UV−O_3 yields a better passivation quality than the N_2O-based oxide layers is not yet clear. One explanation could involve a possible damage to the wafer's surface caused by the plasma treatment. In the case of the combined oxide, this damage would be mitigated by the presence of the UV−O_3 layer on the wafer surface, which agrees with the fact that the passivation quality yielded by the UV−O_3 + N_2O layer is higher than that of the N_2O-only layer. More investigation would need to be carried out to understand this effect. Additionally, further optimization of the process parameters used for the N_2O-plasma treatment might also lead to a higher passivating performance both for the N_2O-only and UV−O_3 + N_2O oxide layers.

Overall, the increased nitrogen and oxygen content in the N_2O-oxide layer appears to widen and shift the optimal processing temperature window toward higher thermal budgets. In the temperature and dwell time ranges analyzed here, the UV−O_3 oxide shows an initial improvement in passivation, followed by a degradation. In contrast, this thermal range marks the lower end of the processing window for the N_2O-grown oxides. This is consistent with contact resistivity trends, where a sharp decrease occurs above a threshold temperature, which is higher for N_2O-based oxides compared to their UV−O_3 counterparts (see Figure 3b). Interestingly, despite the contact resistivity at low thermal budgets being one order of magnitude higher than that of UV−O_3 oxide, it eventually achieves values within the same range as UV−O_3 oxides at high thermal budgets. The XRR and TEM observations showed that the N_2O-oxide maintains its density and structural integrity at the interface at high thermal budgets. The decrease in contact resistivity observed for the N_2O-grown oxides in the high thermal budget range can therefore be attributed to a higher density of active dopants in the SiC_x layer, influencing resistivity at both the c-Si/SiO_x/SiC_x and SiC_x/metal interfaces, rather than to a modification of the N_2O oxide thickness, density or structure. Overall, the integration of the N_2O-oxide in our SiO_x/SiC_x passivating contact enables accessing a wide range of thermal budgets where an optimal balance between high surface passivation and enhanced electrical properties is achieved. We note that we expect the further increase of the processing temperature and dwell time to eventually disrupt the N_2O oxide, leading to a decline in passivation quality, possibly accompanied by a further decrease in contact resistivity.

4. CONCLUSIONS

We have investigated the influence of the annealing thermal budget on passivation quality and contact resistivity of p-type SiO_x/poly-Si passivating contacts with silicon oxide layers obtained through exposure to UV−O_3 or N_2O-plasma in the plasma enhanced chemical vapor deposition (PECVD) chamber. For samples annealed through a rapid thermal processing (RTP), the UV−O_3 oxide exhibited decreasing passivation quality with higher thermal budgets, whereas the N_2O-plasma oxide maintained a stable passivation together with reduced contact resistivity. Combining UV−O_3 and N_2O-plasma oxides showed improved iV_{oc} compared to pure N_2O oxide, possibly due to a reduced surface damage during plasma exposure. Overall, the SiO_x/poly-Si passivating contacts activated both with RTP and through a more conventional tube furnace process showed similar trends with respect to passivation and contact resistivity as a function of the applied thermal budget. This showcases the versatility of the N_2O plasma oxidation process, that resulted in good performance regardless of the thermal profile and annealing setup applied here for poly-Si contact formation. Implementing a process based on N_2O-plasma oxidation (possibly combined with a UV−O_3 process) appears to be a promising strategy to exploit the improved electrical properties that can be obtained at high thermal budget without compromising on the passivation quality. Moreover, it offers the possibility of fabricating SiO_x/poly-Si contacts with a lean process flow using PECVD to deposit both the SiO_x and the poly-Si layers.

The study also involved extensive characterization of the c-Si/SiO_x/poly-Si interface to understand the improved performance of the N_2O-plasma oxide when exposed to high thermal budget compared to the UV−O_3-grown oxide. In particular, from X-ray reflectometry (XRR) and TEM characterizations, we observed the density and structural integrity of the N_2O-plasma oxide to remain stable from low to high thermal budget. In contrast, the UV−O_3 oxide was shown to locally disrupt at high thermal budget, which explains the decrease in passivation observed in this range for samples featuring this oxide. Additional depth-dependent XPS analysis were performed to compare the UV−O_3 and N_2O oxide chemical composition. This analysis revealed that the N_2O-grown oxide contains nitrogen and a higher amount of oxygen compared to its UV−O_3 counterpart. This important finding likely explains the superior thermal stability of the N_2O oxide layer observed in our work as well as by other research institutes.

In a wider context, our findings underscore the effectiveness of the techniques presented here as a robust method for examining multilayer stacks, especially suited for characterizing nanoscale thin films. Notably, we combined more invasive techniques like TEM and XPS depth-profiling with the nondestructive approach of XRR. The results obtained from these various characterization techniques, each relying on different interactions with the samples, consistently align with one another. In our investigation, we conducted the analysis on complete c-Si/SiO_x/poly-Si stacks after annealing. This approach offers the advantage that characterization is performed on samples closely resembling the structures employed in a solar cell application, differing from most similar studies in literature that so far focused on as-deposited SiO_x layers.

https://doi.org/10.1021/acsami.4c10612
ACS Appl. Mater. Interfaces 2024, 16, 47931−47943

■ ASSOCIATED CONTENT

Data Availability Statement

The data underlying this contribution is available on the on the Zenodo repository associated with the following DOI: 10.5281/zenodo.13272021.

Supporting Information

The Supporting Information is available free of charge at https://pubs.acs.org/doi/10.1021/acsami.4c10612.

iV_{oc} and ρ_C data for N_2O-grown oxides as a function of plasma time and pressure in the PECVD chamber (Figures S1 and S2); iV_{oc} and ρ_C data for N_2O-only and UV−O_3 + N_2O oxides as a function of RTP temperatures with dwell time of 30 s (Figure S3); photoluminescence imaging of samples with optimized UV−O_3, N_2O, and UV−O_3 + N_2O oxide layers (Figure S4); active doping concentrations measured by ECV for long-annealed samples with the three different oxide types and different annealing conditions (Figure S5); STEM-EELS scans of the interface of N_2O and UV−O_3 oxide samples (Figure S6); contour plot of depth-dependent XPS data for UV−O_3 and N_2O oxide samples (Figure S7); parameters obtained from the fit of the X-ray reflectograms (Table S1), and XPS data and fit for Si 2p, O 1s, and N 1s spectral ranges for UV−O_3 and N_2O samples (Figure S8) (PDF)

■ AUTHOR INFORMATION

Corresponding Authors

Sofia Libraro − *Ecole Polytechnique Fédérale de Lausanne (EPFL), Institute of Electrical and Microengineering (IEM), Photovoltaics and Thin-Film Electronics Laboratory (PV-Lab), 2000 Neuchâtel, Switzerland*; Email: sofia.libraro@epfl.ch

Audrey Morisset − *Ecole Polytechnique Fédérale de Lausanne (EPFL), Institute of Electrical and Microengineering (IEM), Photovoltaics and Thin-Film Electronics Laboratory (PV-Lab), 2000 Neuchâtel, Switzerland; CSEM Sustainable Energy Center, 2002 Neuchâtel, Switzerland*; orcid.org/0000-0003-0878-6725; Email: audrey.morisset@csem.ch

Authors

Lars J. Bannenberg − *Department of Radiation Science and Technology, Faculty of Applied Sciences, Delft University of Technology, 2629JB Delft, The Netherlands*; orcid.org/0000-0001-8150-3694

Theodosios Famprikis − *Department of Radiation Science and Technology, Faculty of Applied Sciences, Delft University of Technology, 2629JB Delft, The Netherlands*; orcid.org/0000-0002-7946-1445

David Reyes − *Interdisciplinary Centre for Electron Microscopy, EPFL, 1015 Lausanne, Switzerland*

Julien Hurni − *Ecole Polytechnique Fédérale de Lausanne (EPFL), Institute of Electrical and Microengineering (IEM), Photovoltaics and Thin-Film Electronics Laboratory (PV-Lab), 2000 Neuchâtel, Switzerland*

Ezgi Genc − *Ecole Polytechnique Fédérale de Lausanne (EPFL), Institute of Electrical and Microengineering (IEM), Photovoltaics and Thin-Film Electronics Laboratory (PV-Lab), 2000 Neuchâtel, Switzerland*

Christophe Ballif − *Ecole Polytechnique Fédérale de Lausanne (EPFL), Institute of Electrical and Microengineering (IEM), Photovoltaics and Thin-Film Electronics Laboratory (PV-Lab), 2000 Neuchâtel, Switzerland; CSEM Sustainable Energy Center, 2002 Neuchâtel, Switzerland*

Aïcha Hessler-Wyser − *Ecole Polytechnique Fédérale de Lausanne (EPFL), Institute of Electrical and Microengineering (IEM), Photovoltaics and Thin-Film Electronics Laboratory (PV-Lab), 2000 Neuchâtel, Switzerland*

Franz-Josef Haug − *Ecole Polytechnique Fédérale de Lausanne (EPFL), Institute of Electrical and Microengineering (IEM), Photovoltaics and Thin-Film Electronics Laboratory (PV-Lab), 2000 Neuchâtel, Switzerland*

Complete contact information is available at: https://pubs.acs.org/10.1021/acsami.4c10612

Notes

The authors declare no competing financial interest.

■ ACKNOWLEDGMENTS

The authors gratefully acknowledge financial support by the Swiss National Science Foundation (SNF) for the project IMPACT (grant No. 200021_185064), by the Swiss Federal Office for Energy (OFEN) within the project iPrecise (SI/502115-01) as well as from the European Union's Horizon 2020 and Horizon Europe research and innovation programs under the Marie Skłodowska-Curie grant agreement nos. 101028491 (A.M.) and 101066486 (T.F.), respectively. Xavier Niquille is thanked for the wet chemical cleaning of the wafers, and Joël Spitznagel is thanked for support to sample fabrication. Bart Boshuizen is kindly acknowledged for supporting the XPS measurements.

■ REFERENCES

(1) Feldmann, F.; Bivour, M.; Reichel, C.; Hermle, M.; Glunz, S. W. Passivated Rear Contacts for High-Efficiency n-Type Si Solar Cells Providing High Interface Passivation Quality and Excellent Transport Characteristics. *Sol. Energy Mater. Sol. Cells* **2014**, *120* (Part A), 270−274.

(2) JinkoSolar JinkoSolar's High-efficiency N-Type Monocrystalline Silicon Solar Cell Sets Our New Record with Maximum Conversion Efficiency of 26.4%, 2024 https://www.prnewswire.com/news-releases/jinkosolars-high-efficiency-n-type-monocrystalline-silicon-solar-cell-sets-our-new-record-with-maximum-conversion-efficiency-of-26-4-301700102.html. (accessed June 25, 2024).

(3) Feldmann, F.; Simon, M.; Bivour, M.; Reichel, C.; Hermle, M.; Glunz, S. W. Efficient Carrier-Selective p- and n-Contacts for Si Solar Cells. *Sol. Energy Mater. Sol. Cells* **2014**, *131*, 100−104.

(4) Gan, J. Y.; Swanson, R. M. In *Polysilicon Emitters for Silicon Concentrator Solar Cells*, IEEE Conference on Photovoltaiv Specialists; IEEE, 1990; pp 245−250.

(5) Römer, U.; Peibst, R.; Ohrdes, T.; Lim, B.; Krügener, J.; Bugiel, E.; Wietler, T.; Brendel, R. Recombination Behavior and Contact Resistance of N+ and P+ Poly-Crystalline Si/Mono-Crystalline Si Junctions. *Sol. Energy Mater. Sol. Cells* **2014**, *131*, 85−91.

(6) Nogay, G.; Stuckelberger, J.; Wyss, P.; Rucavado, E.; Allebé, C.; Koida, T.; Morales-Masis, M.; Despeisse, M.; Haug, F. J.; Löper, P.; Ballif, C. Interplay of Annealing Temperature and Doping in Hole Selective Rear Contacts Based on Silicon-Rich Silicon-Carbide Thin Films. *Sol. Energy Mater. Sol. Cells* **2017**, *173*, 18−24.

(7) Yan, D.; Cuevas, A.; Phang, S. P.; Wan, Y.; Macdonald, D. 23% Efficient P-Type Crystalline Silicon Solar Cells with Hole-Selective Passivating Contacts Based on Physical Vapor Deposition of Doped Silicon Films. *Appl. Phys. Lett.* **2018**, *113* (6), No. 061603, DOI: 10.1063/1.5037610.

(8) Linke, J.; Glatthaar, R.; Huster, F.; Okker, T.; Möller, S.; Hahn, G.; Terheiden, B. Poly-Si Thickness and Temperature Dependent

Oxide Disruption Induced by Penetration of the Interfacial Oxide in (p) Poly-Si/SiOx Passivating Contacts. *Sol. Energy Mater. Sol. Cells* **2022**, *246*, No. 111890.
(9) Nogay, G.; Stuckelberger, J.; Wyss, P.; Jeangros, Q.; Allebé, C.; Niquille, X.; Debrot, F.; Despeisse, M.; Haug, F. J.; Löper, P.; Ballif, C. Silicon-Rich Silicon Carbide Hole-Selective Rear Contacts for Crystalline-Silicon-Based Solar Cells. *ACS Appl. Mater. Interfaces* **2016**, *8* (51), 35660−35667.
(10) Polzin, J. I.; Lange, S.; Richter, S.; Moldovan, A.; Bivour, M.; Hagendorf, C.; Hermle, M.; Glunz, S. W.; Feldmann, F. Temperature-Induced Stoichiometric Changes in Thermally Grown Interfacial Oxide in Tunnel-Oxide Passivating Contacts. *Sol. Energy Mater. Sol. Cells* **2020**, *218*, No. 110713.
(11) Morisset, A.; Cabal, R.; Giglia, V.; Boulineau, A.; De Vito, E.; Chabli, A.; Dubois, S.; Alvarez, J.; Kleider, J. P. Evolution of the Surface Passivation Mechanism during the Fabrication of Ex-Situ Doped Poly-Si(B)/SiOx Passivating Contacts for High-Efficiency c-Si Solar Cells. *Sol. Energy Mater. Sol. Cells* **2021**, *221*, No. 110899.
(12) Asuha, H. K.; Maida, O.; Takahashi, M.; Iwasa, H. Nitric Acid Oxidation of Si to Form Ultrathin Silicon Dioxide Layers with a Low Leakage Current Density. *J. Appl. Phys.* **2003**, *94* (11), 7328−7335.
(13) Feldmann, F.; Müller, R.; Reichel, C.; Hermle, M. Ion Implantation into Amorphous Si Layers to Form Carrier-Selective Contacts for Si Solar Cells. *Phys. Status Solidi RRL* **2014**, *08* (9), 767−770.
(14) Moldovan, A.; Feldmann, F.; Zimmer, M.; Rentsch, J.; Benick, J.; Hermle, M. Tunnel Oxide Passivated Carrier-Selective Contacts Based on Ultra-Thin SiO2 Layers. *Sol. Energy Mater. Sol. Cells* **2015**, *142*, 123−127.
(15) Morisset, A.; Cabal, R.; Grange, B.; Marchat, C.; Alvarez, J.; Gueunier-Farret, M. E.; Dubois, S.; Kleider, J. P. Highly Passivating and Blister-Free Hole Selective Poly-Silicon Based Contact for Large Area Crystalline Silicon Solar Cells. *Sol. Energy Mater. Sol. Cells* **2019**, *200*, No. 109912.
(16) Moldovan, A.; Feldmann, F.; Krugel, G.; Zimmer, M.; Rentsch, J.; Hermle, M.; Roth-Fölsch, A.; Kaufmann, K.; Hagendorf, C. Simple Cleaning and Conditioning of Silicon Surfaces with UV/Ozone Sources. *Energy Procedia* **2014**, *55*, 834−844, DOI: 10.1016/j.egypro.2014.08.067.
(17) Wu, Y.; Stodolny, M. K.; Geerligs, L. J.; Lenes, M.; Luchies, J. M. In-Situ Doping and Local Overcompensation of High Performance LPCVD Polysilicon Passivated Contacts as Approach to Industrial IBC Cells. *Energy Procedia* **2016**, *92*, 427−433, DOI: 10.1016/j.egypro.2016.07.123.
(18) Fong, K. C.; Kho, T. C.; Liang, W. S.; Chong, T. K.; Ernst, M.; Walter, D.; Stocks, M.; Franklin, E.; McIntosh, K.; Blakers, A. Phosphorus Diffused LPCVD Polysilicon Passivated Contacts with In-Situ Low Pressure Oxidation. *Sol. Energy Mater. Sol. Cells* **2018**, *186*, 236−242.
(19) Deal, B. E.; Grove, A. S. General Relationship for the Thermal Oxidation of Silicon. *J. Appl. Phys.* **1965**, *36* (12), 3770−3778.
(20) Khalilov, U.; Neyts, E. C.; Pourtois, G.; Van Duin, A. C. T. Can We Control the Thickness of Ultrathin Silica Layers by Hyperthermal Silicon Oxidation at Room Temperature? *J. Phys. Chem. C* **2011**, *115* (50), 24839−24848.
(21) Khalilov, U.; Pourtois, G.; Huygh, S.; van Duin, A. C. T.; Neyts, E. C.; Bogaerts, A. New Mechanism for Oxidation of Native Silicon Oxide. *J. Phys. Chem. C* **2013**, *117* (19), 9819−9825.
(22) van der Vossen, R.; Feldmann, F.; Moldovan, A.; Hermle, M. Comparative Study of Differently Grown Tunnel Oxides for P-Type Passivating Contacts. *Energy Procedia* **2017**, *124*, 448−454, DOI: 10.1016/j.egypro.2017.09.273.
(23) Jeon, M.; Kang, J.; Shim, G.; Ahn, S.; Balaji, N.; Park, C.; Lee, Y. J.; Yi, J. Passivation Effect of Tunnel Oxide Grown by N2O Plasma for C-Si Solar Cell Applications. *Vacuum* **2017**, *141*, 152−156.
(24) Huang, Y.; Liao, M.; Wang, Z.; Guo, X.; Jiang, C.; Yang, Q.; Yuan, Z.; Huang, D.; Yang, J.; Zhang, X.; Wang, Q.; Jin, H.; Al-Jassim, M.; Shou, C.; Zeng, Y.; Yan, B.; Ye, J. Ultrathin Silicon Oxide Prepared by In-Line Plasma-Assisted N2O Oxidation (PANO) and the Application for n-Type Polysilicon Passivated Contact. *Sol. Energy Mater. Sol. Cells* **2020**, *208*, No. 110389.
(25) Stöhr, M.; Aprojanz, J.; Brendel, R.; Dullweber, T. Firing-Stable PECVD SiO XN y/n-Poly-Si Surface Passivation for Silicon Solar Cells. *ACS Appl. Energy Mater.* **2021**, *4* (5), 4646−4653.
(26) Xing, H.; Liu, Z.; Yang, Z.; Liao, M.; Wu, Q.; Lin, N.; Liu, W.; Ding, C.; Zeng, Y.; Yan, B.; Ye, J. Plasma Treatment for Chemical SiOx Enables Excellent Passivation of P-Type Polysilicon Passivating Contact Featuring the Lowest J0 of ∼ 6 FA/Cm2. *Sol. Energy Mater. Sol. Cells* **2023**, *257*, No. 112354.
(27) Glunz, S. W.; Steinhauser, B.; Polzin, J. I.; Luderer, C.; Grübel, B.; Niewelt, T.; Okasha, A. M. O. M.; Bories, M.; Nagel, H.; Krieg, K.; Feldmann, F.; Richter, A.; Bivour, M.; Hermle, M. Silicon-Based Passivating Contacts: The TOPCon Route. *Prog. Photovoltaics* **2023**, *31* (4), 341−359.
(28) Masuda, A.; Morimoto, A.; Kumeda, M.; Shimizu, T.; Yonezawa, Y.; Minamikawa, T. Novel Oxidation Process of Hydrogenated Amorphous Silicon Utilizing Nitrous Oxide Plasma. *Appl. Phys. Lett.* **1992**, *61* (7), 816−818.
(29) Yao, Z.; Yang, G.; Han, C.; Moya, P. P.; Özkol, E.; Yan, J.; Zhao, Y.; Cao, L.; van Swaaij, R.; Mazzarella, L.; Isabella, O. Poly-SiOx Passivating Contacts with Plasma-Assisted N2O Oxidation of Silicon (PANO-SiOx). *Sol. RRL* **2023**, *7* (18), No. 2300186, DOI: 10.1002/solr.202300186.
(30) Lee, D. R.; Lucovsky, G.; Denker, M. S.; Magee, C. Nitrogen-Atom Incorporation at Si−SiO2 Interfaces by a Low-Temperature (300 °C), Pre-Deposition, Remote-Plasma Oxidation Using N2O. *J. Vac. Sci. Technol., A* **1995**, *13* (3), 1671−1675.
(31) Mertens, V.; Dorn, S.; Langlois, J.; Stöhr, M.; Larionova, Y.; Veurman, W.; Brendel, R.; Ambrosius, N.; Vogt, A.; Pernau, T.; Haverkamp, H.; Dullweber, T. Plasma-Enhanced Chemical-Vapor-Deposited SiOx(Ny)/n-Type Polysilicon-on-Oxide-Passivating Contacts in Industrial Back-Contact Si Solar Cells. *Sol. RRL* **2024**, *8* (12), No. 2300919, DOI: 10.1002/solr.202300919.
(32) Ingenito, A.; Nogay, G.; Jeangros, Q.; Rucavado, E.; Allebé, C.; Eswara, S.; Valle, N.; Wirtz, T.; Horzel, J.; Koida, T.; Morales-Masis, M.; Despeisse, M.; Haug, F. J.; Löper, P.; Ballif, C. A Passivating Contact for Silicon Solar Cells Formed during a Single Firing Thermal Annealing. *Nat. Energy* **2018**, *3* (9), 800−808.
(33) Haug, F.-J.; Ingenito, A.; Meyer, F.; Libraro, S.; Bolis, N.; Leon, J. J. D.; Allebé, C.; Ballif, C. Contributions to the Contact Resistivity in Fired Tunnel-Oxide Passivating Contacts for Crystalline Silicon Solar Cells. *IEEE J. Photovoltaics* **2019**, *9* (6), 1548−1553, DOI: 10.1109/JPHOTOV.2019.2939880.
(34) David, L.; Hübner, S.; Min, B.; Hollemann, C.; Dippell, T.; Wohlfart, P.; Peibst, R.; Brendel, R.Fired-Only Passivating Poly-Si on Oxide Contacts with DC-Sputtered In Situ Phosphorous-Doped Silicon Layers. In *37th European Photovoltaic Solar Energy Conference and Exhibition*; EU PVSEC, 2020; pp 184−187.
(35) Ingenito, A.; Libraro, S.; Wyss, P.; Allebé, C.; Despeisse, M.; Nicolay, S.; Haug, F. J.; Ballif, C. Implementation and Understanding of P+ Fired Rear Hole Selective Tunnel Oxide Passivating Contacts Enabling > 22% Conversion Efficiency in P-Type c-Si Solar Cells. *Sol. Energy Mater. Sol. Cells* **2021**, *219*, No. 110809.
(36) Lehmann, M.; Valle, N.; Horzel, J.; Pshenova, A.; Wyss, P.; Döbeli, M.; Despeisse, M.; Eswara, S.; Wirtz, T.; Jeangros, Q.; Hessler-Wyser, A.; Haug, F. J.; Ingenito, A.; Ballif, C. Analysis of Hydrogen Distribution and Migration in Fired Passivating Contacts (FPC). *Sol. Energy Mater. Sol. Cells* **2019**, *200*, No. 110018.
(37) Eidelloth, S.; Brendel, R. Analytical Theory for Extracting Specific Contact Resistances of Thick Samples from the Transmission Line Method. *IEEE Electron Device Lett.* **2014**, *35* (1), 9−11.
(38) Glavic, A.; Björck, M. GenX 3: The Latest Generation of an Established Tool. *J. Appl. Crystallogr.* **2022**, *55*, 1063−1071.
(39) Morisset, A.; Famprikis, T.; Haug, F. J.; Ingenito, A.; Ballif, C.; Bannenberg, L. J. In Situ Reflectometry and Diffraction Investigation of the Multiscale Structure of P-Type Polysilicon Passivating Contacts for c-Si Solar Cells. *ACS Appl. Mater. Interfaces* **2022**, *14* (14), 16413−16423.

(40) Libraro, S.; Morisset, A.; Hurni, J.; Genç, E.; Antognini, L.; Bannenberg, L. J.; Famprikis, T.; Ballif, C.; Hessler-Wyser, A.; Haug, F. J. Understanding and Mitigating Resistive Losses in Fired Passivating Contacts: Role of the Interfaces and Optimization of the Thermal Budget. *Sol. Energy Mater. Sol. Cells* **2023**, *263*, No. 112591.
(41) Chastain, J. *Handbook of X-Ray Photoelectron Spectroscopy*; Perkin-Elmer Corporation, 1992.
(42) Grunthaner, P. J.; Hecht, M. H.; Grunthaner, F. J.; Johnson, N. M. The Localization and Crystallographic Dependence of Si Suboxide Species at the SiO2/Si Interface. *J. Appl. Phys.* **1987**, *61* (2), 629−638.
(43) Shallenberger, J. R. Determination of Chemistry and Microstructure in SiO x (0.1< x <0.8) Films by x-Ray Photoelectron Spectroscopy. *J. Vac. Sci. Technol., A* **1996**, *14* (3), 693−698.
(44) Alfonsetti, R.; Lozzi, L.; Passacantando, M.; Picozzi, P.; Santucci, S. XPS Studies on SiOx Thin Films. *Appl. Surf. Sci.* **1993**, *70*−*71* (Part 1), 222−225.

https://doi.org/10.1021/acsami.4c10612
ACS Appl. Mater. Interfaces 2024, 16, 47931−47943